Ligand-Mediated Band Engineering in Bottom-Up Assembled SnTe Nanocomposites for Thermoelectric Energy Conversion

Maria Ibáñez,[#,†,‡,*] Roger Hasler,[†,‡] Aziz Genç,[‖,§] Yu Liu,[#] Beatrice Kuster,[†,‡] Maximilian Schuster,[†] Oleksandr Dobrozhan,[⊥] Doris Cadavid,[⊥] Jordi Arbiol,[§,¶] Andreu Cabot,[⊥,¶] and Maksym V. Kovalenko[†,‡,*]

\# Institute of Science and Technology Austria, Am Campus 1, 3400 Klosterneuburg, Austria

† Institute of Inorganic Chemistry, Department of Chemistry and Applied Biosciences, ETH Zürich, Vladimir Prelog Weg 1, CH-8093, Switzerland

‡ Empa-Swiss Federal Laboratories for Materials Science and Technology, Dübendorf, Überlandstrasse 129, CH-8600, Switzerland

‖ Department of Metallurgy and Materials Engineering, Faculty of Engineering, Bartin University, 74100 Bartin, Turkey

§ Catalan Institute of Nanoscience and Nanotechnology (ICN2), CSIC and BIST, Campus UAB, Bellaterra, 08193 Barcelona, Catalonia, Spain

⊥ Catalonia Energy Research Institute - IREC, Sant Adria del Besos, 08930 Barcelona, Spain

¶ ICREA, Pg. Lluís Companys 23, 08010 Barcelona, Spain

* mibanez@ist.ac.at, kovalenko@ethz.ch

Contents

1. Chemicals

Tin(II) bromide ($SnBr_2$, 99%) and N-methylformamide (MFA, 99%) was purchased from ABCR. Tellurium (Te, shot 1-2 mm, 99.999%), selenium (Se, pellets, <5 mm particle size, ≥99.999% trace metals basis), oleic acid (OA, 90%, technical grade), 1-octadecene (ODE, 90%, technical grade), 1,2-ethylenediamine (en, puriss. p.a., absolute, ≥99.5% , GC), 1,2-ethanedithiol ($edtH_2$, >98%), were purchased from Sigma Aldrich. Oleylamine (OLA, min. 95%) and tri-n-octylphosphine were purchased from Strem Chemicals. Trioctylamine (TOA, ≥ 93%) was purchased from Merck.

Anhydrous hexane, ethanol, 2-propanol, tetrahydrofuran (THF), acetonitrile (ACN) and acetone were obtained from various sources. All chemicals were used as received without purification, except for MFA, $edtH_2$ and en. MFA was dried over 4 Å molecular sieves at room temperature under an Ar-flow for 20 h and then filtered using syringe filters (PTFE, 0.45 μm). $edtH_2$ was dried over activated 4 Å molecular sieves (>3 days) followed by decantation and distillation under nitrogen discarding the first fraction. en was pre-dried for 5 days with CaH_2 (approx. 20 g/l), followed by decantation, refluxing over Na (19 h), then distillation (at 116°C). The distilled en was stored in the glovebox over activated 4 Å molecular sieves and filtered using 0.45 μm PTFE syringe filters before usage.

2. SnTe NCs synthesis

To avoid all possible sources for oxidation, all syntheses were carried out using standard air-free techniques and the washing procedures of all NCs were done in the glovebox.

In advance of the synthesis, tellurium (5.08 g, 0.04 mol) was dissolved in trioctylphosphine (20 ml) by stirring in a glovebox to yield a 2 M tellurium precursor solution (TOP:Te). The complete dissolution could take up to a week. The final solution was filtered using 0.45 μm PTFE syringe filters.

Tin (II) bromide (1.67 g, 6 mmol) was mixed with trioctylamine (24 ml), oleylamine (24 ml) and 1-octadecene (12 ml) under argon flow. The mixture was degassed under vacuum by stirring at room temperature, 60 °C and 100 °C for 30 min each. Subsequently, the vacuum was replaced with argon flow and the reaction mixture was heated to 160 °C. 3 ml of 2 M TOP:Te was rapidly injected, and the temperature was raised to 240 °C. The reaction mixture was maintained for 20 minutes at 240 °C, and then then quickly cooled down to room temperature using a water bath. **Comment on washing:** The obtained NCs were precipitated from the reaction solution by centrifugation (5 min, 12100 rpm). The precipitated NCs were re-dispersed in tetrahydrofuran and washed one more time by addition of acetonitrile, followed by centrifugation (3 min, 4400 rpm). The washed NCs were directly re-dispersed in hexane and the concentration was determined by the weight of an aliquot after solvent evaporation.

3. CdSe ligand preparation

To avoid all possible sources for oxidation, all ligand exchange procedures were carried out in the glovebox.

The CdSe-based ligand (125 mg) was obtained by mixing stoichiometric amounts of elemental Cd (74 mg) and Se (52 mg) with en (2 ml) and $edtH_2$ (0.2 ml) in the glovebox. The mixture was stirred at room temperature until complete dissolution (usually within a couple of hours the compounds are completely dissolved). CdSe-based ligand was prepared a few hours before the ligand exchange was conducted, due to limited stability (partial precipitation after 24 h after dissolution).

Upon recrystallization at 350 °C on a glass substrate, the material was analyzed by X-ray diffraction (XRD). The diffractogram obtained matches to hexagonal CdSe phase corresponding to the JCPDS-ICDD card no. 00-077-2307 (Figure S1).
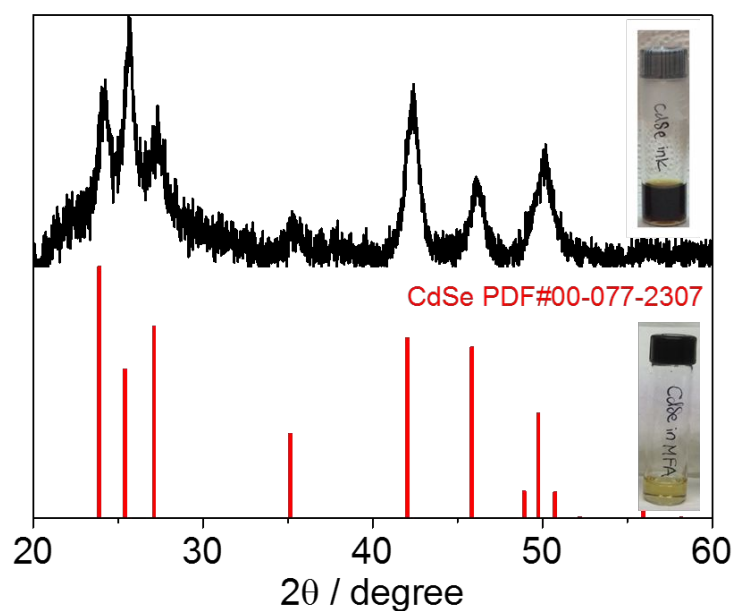
Figure S1. XRD diffraction pattern of re-crystallized CdSe-based ligand. Top picture of the vial is a concentrated solution of CdSe in the amine-thiol mixture. Bottom picture of the vial is the diluted solution of CdSe ligand used for the ligand exchange.

4. Ligand exchange with CdSe-complexes

In order to replace the organic ligands on the surface of SnTe NCs by the CdSe ligand previously prepared, we used a phase transfer procedure. A solution of the CdSe-based ligand (24 µL/mL) in MFA was prepared in an argon-filled glovebox. An equal volume of a suspension of SnTe NCs (10 mg/mL) in hexane was layered on top of the polar phase. This mixture was stirred at room temperature for 16 h. A phase transfer of the NCs from the non-polar to the polar phase was achieved as evidenced by the colorless hexane phase and colored MFA phase. The top hexane phase was then fully extracted and the NCs were precipitated by centrifugation. The obtained NCs were washed twice with acetone and dried under vacuum until obtaining a fine powder.

4. Pellet fabrication

NCs powders were pressed using a custom-made hot press. In this system, the heat is provided by an induction coil operated in the RF range applied directly to a graphite die acting as a susceptor. This setup configuration allows increasing temperature at a similar rate than Spark Plasma Sintering (SPS). Inside a glovebox, NC-based powder were ground and loaded into a 10 mm diameter graphite die lined with 0.13 mm thick graphite paper. The filled die was placed in the hot press system. The densification profile applied an axial pressure of 40 MPa before heating the die. The density of the pressed pellets was measured by the Archimedes method.

Note: A two-step process was used for the annealing. First at 210 °C to warrant the complete evaporation of the physisorbed MFA; and later at 450 °C during 1 h. Thereafter, the obtained nanopowders were consolidated by applying an axial pressure of 40 MPa at 450 °C for 5 minutes. All consolidated pellets presented relative densities above 93 % of their theoretical value. After consolidation, materials were annealed at 580 °C to warranty stability in the whole temperature range of the measurements.

Note2: The pressing conditions were chosen to obtain densities above 90% of the theoretical values. In particular, we used pressures of 40 MPa, higher pressure end up damaging the graphite die. The temperature was chosen 450 ˚C since lower temperatures yield pellets with densities below 90%. Higher temperatures were discarded

since they didn't significantly increase the density and they could induce further crystal growth during consolidation.

5. Characterization

5.1. X-Ray Diffraction (XRD)

XRD analysis was done directly on the as-synthesised NCs before and after the ligand exchange treatment as well as after the consolidation into pellets. The measurements were done in a Bruker D8 Advance powder diffractometer equipped with a M. Braun 50 m position sensitive detector, Bragg-Brentano geometry, Cu Kalpha1 radiation (1.54059 Å), focussing Ge-monochromator.
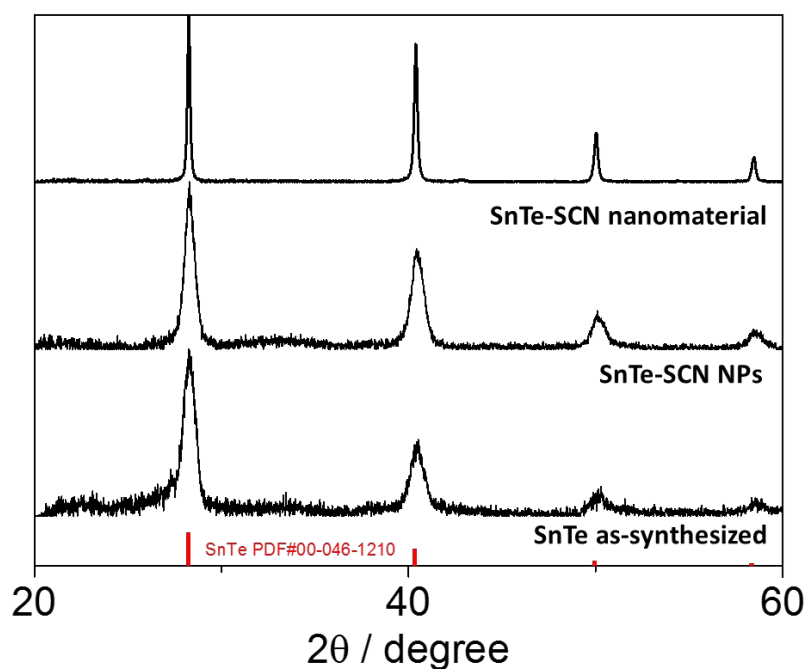

Figure S2. Powder XRD pattern of as-synthetized SnTe NCs, SnTe NCs capped with SCN (SnTe-SCN NPs); and SnTe-SCN nanomaterial obtained after hot pressing the sample at 450 °C. *Note:* Based on ICP results as well as on the absence of any shift from the XRD pattern we speculate that no sulfur remains from the ligand after the heat treatment and hot-pressing.
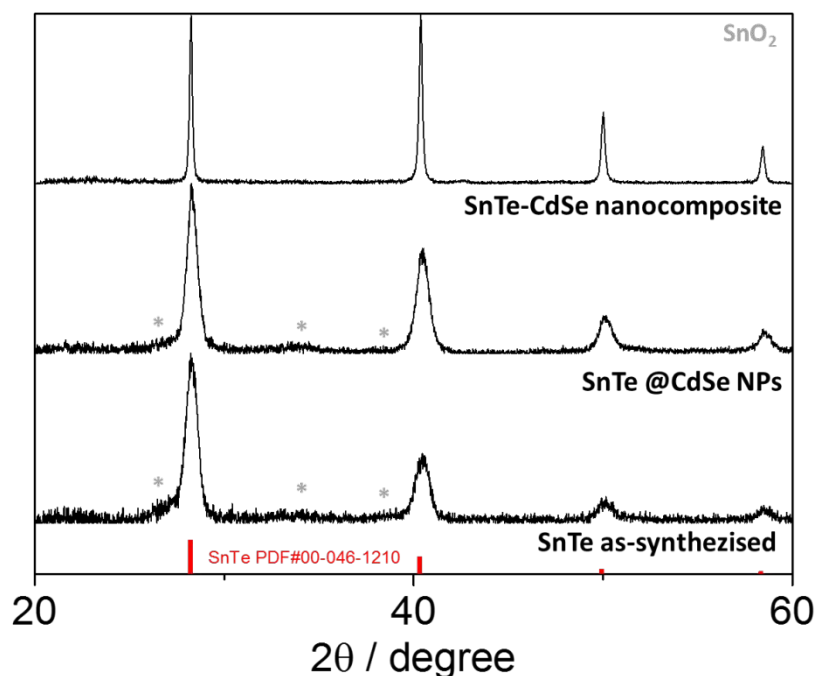
Figure S3. Powder XRD pattern of as-synthetized SnTe NCs, SnTe NCs capped with CdSe-based ligand (SnTe@CdSe NPs); and SnTe-CdSe nanocomposite obtained after hot pressing the sample at 450 °C. *Note:* The XRD analysis, show a peak shift towards lower angles which would be expected for partial Cd-alloying.

5.3 Transmission electron microscopy

HRTEM and STEM studies were conducted using a FEI Tecnai F20 field emission gun microscope operated at 200 kV with a point-to-point resolution of 0.19 nm, which is equipped with high-angle annular dark field and energy-dispersive X-ray spectroscopy detectors and a Quantum Gatan Image Filter (Quantum GIF) for the electron energy-loss spectroscopy (EELS) analyses. Atomic resolution STEM images of the powders were obtained by using a probe corrected FEI Titan 60−300 equipped with a high brightness field emission gun (XFEG) and a CETCOR corrector from CEOS, producing a probe size of about 1 Å.

TEM samples were prepared as the following: (i) For the SnTe@CdSe NPs, solutions containing the NP were dropped over a carbon coated copper grid and dried in ambient conditions, (ii) For the pellet, we prepared a cross-section by cutting it with a diamond saw. The piece obtained was afterwards mechanically thinned to 20-30 μm and further thinned to electron transparency by Ar^+ polishing using a Gatan Precision Ion Polishing System.

5.4. Electrical properties

The pressed samples were polished, maintaining the disk-shape morphology. Final pellets had a 10 mm diameter and were approximately 1 mm thick. The Seebeck coefficient was measured using a static DC method. Electrical resistivity data were obtained by a standard four-probe method. Both the Seebeck coefficient and the electrical resistivity were simultaneously measured with accuracies better than 1% in a LSR-3 LINSEIS system from room temperature to 850 K, under helium atmosphere. Samples were held between two alumel electrodes and two probe thermocouples with spring-loaded pressure contacts. Additional, due to the high temperature reach during the measurements, the samples were spray coated with boron nitride to minimize out-degassing except where needed for electrical contact with the thermocouples, heater and voltage probes. A resistive heater on the lower electrode created temperature differentials in the sample to determine the Seebeck coefficient. Hall carrier

concentrations were measured using a PPMS-9T from Quantum Design, Inc. at room temperature under a magnetic field of 2 T.

Note: The results presented in the manuscript are an average of the results obtained after measuring 3 pellets produced under identical conditions. The measurements between different samples had standard deviations below 10 %. Additionally each pellet has been measured 3 times providing no hysteresis between the heating and cooling cycles (Figure S4). The major difference was found between the up and down of the first cycle. Afterwards, the values remain stable. Therefore all the measurements presented in the manuscript correspond to the heating cycle of the 2nd measurement.
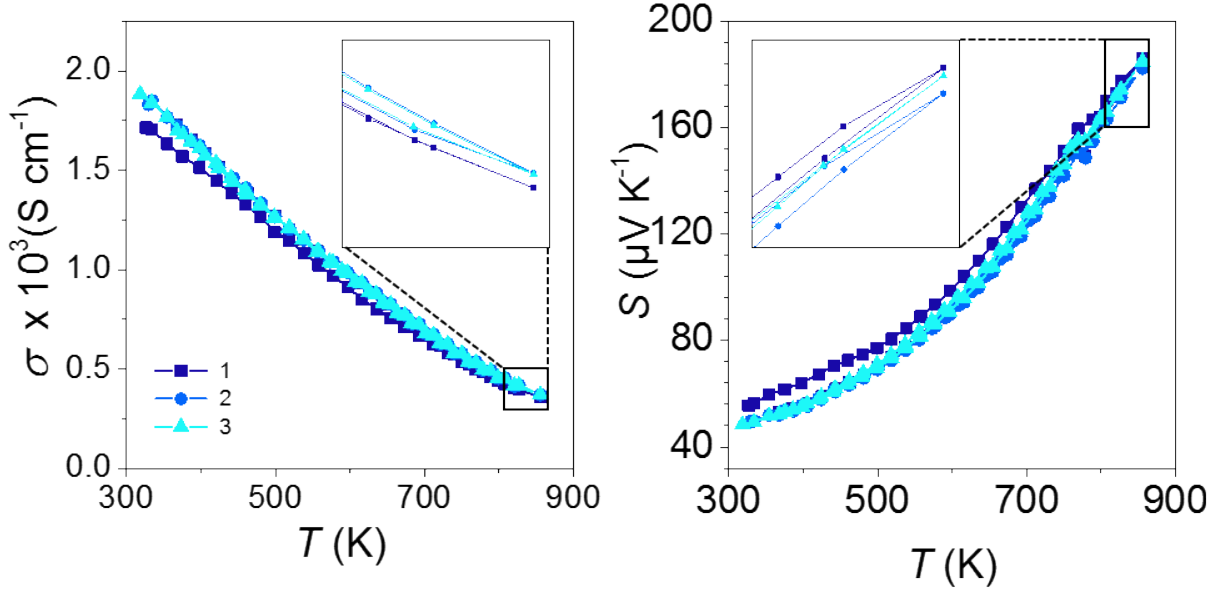

Figure S4. Temperature dependence of the electrical conductivity, and Seebeck coefficient of SnTe-CdSe nanocomposite measured 3 consecutive times during heating up and cooling down to 856 K.

5.5 Thermal properties

An XFA 600 Xenon Flash Apparatus was used to determine the thermal diffusivities of all samples with an accuracy of *ca.* 6%. Total thermal conductivity (κ) was calculated using the relation $\kappa = DC_p\rho$, where D is the thermal diffusivity, C_p is the heat capacity and ρ is the mass density of the pellet. The ρ values were calculated using the Archimedes method. The value used for the heat capacity was from the Dulong-Petit limit. The electronic contribution of the thermal conductivity was calculated using the Wiedemann–Franz law, taking as the Lorenz number 1.49×10^{-8} V^2K^{-2} which is commonly used for metals and non-degenerate semiconductors

6. Notes

6.1. Elemental mapping of SnTe@CdSe NPs

The EELS compositional maps presented in the main text were obtained with a dispersion of 1 eV/channel covering all four elements. In the following elemental mapping, we used a dispersion of 0.5 eV/channel during the EELS analyses in order to get the best possible resolution covering the various edges of Sn, Te and Cd. However, due to spectral range required (1000 eV difference between the peaks of Cd and Se), we cannot present the Se elemental map along Sn, Te and Cd at these conditions.
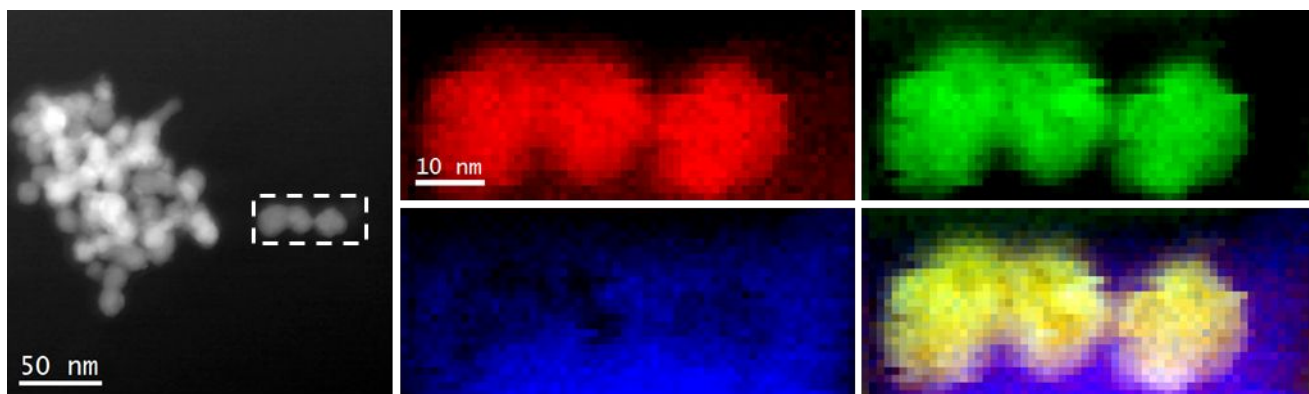

Figure S5. ADF STEM micrograph of some SnTe@CdSe NPs. STEM–EELS elemental composition maps of the area indicated with a white rectangle: Sn (red), Te (green), and Cd (blue) along with their composite.
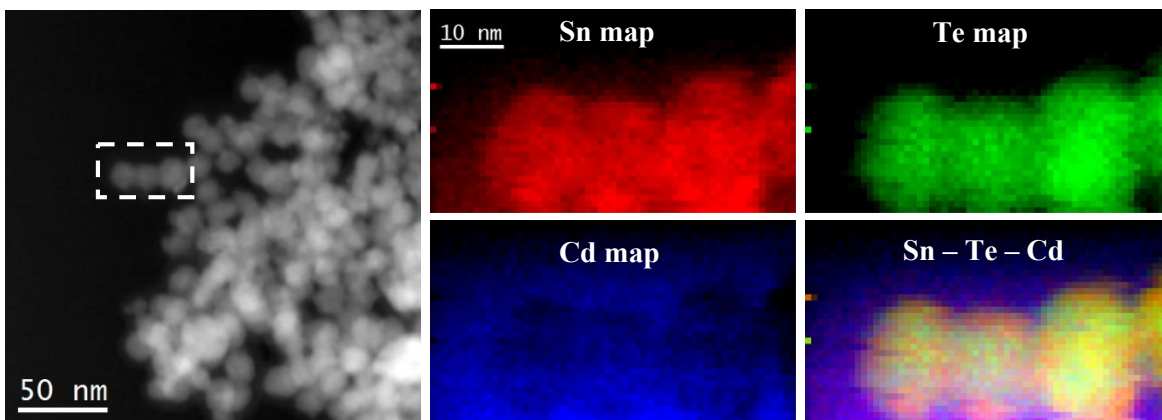

Figure S6. ADF STEM micrograph of a different group of SnTe@CdSe NPs. STEM – EELS elemental composition maps of the area indicated with a white rectangle: Sn (red), Te (green) and Cd (blue) along with their composite.

Figure S5 and S6 show ADF STEM micrographs and the corresponding STEM-EELS analyses of the indicated area. Elemental composition maps of Sn (red), Te (green), Cd (blue) and Se (yellow) along with the composites of Sn – Te, Sn – Cd, Cd – Se and Cd – Te are shown in this figure. In general, we can see that the cores of the nanoparticles are richer in Sn and Te, and the surrounding is composed of Cd and Se.

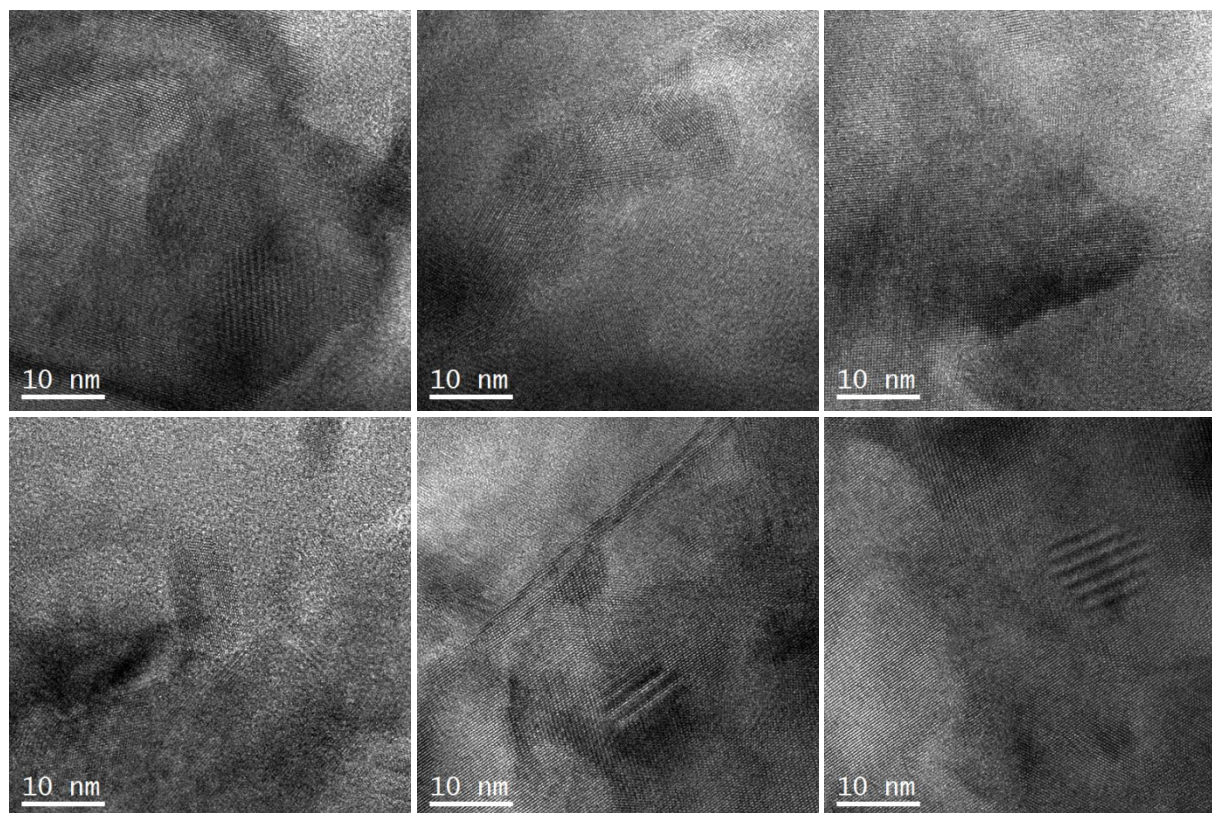**6.2. Nanometric structural characterization of SnTe-CdSe nanocomposites**

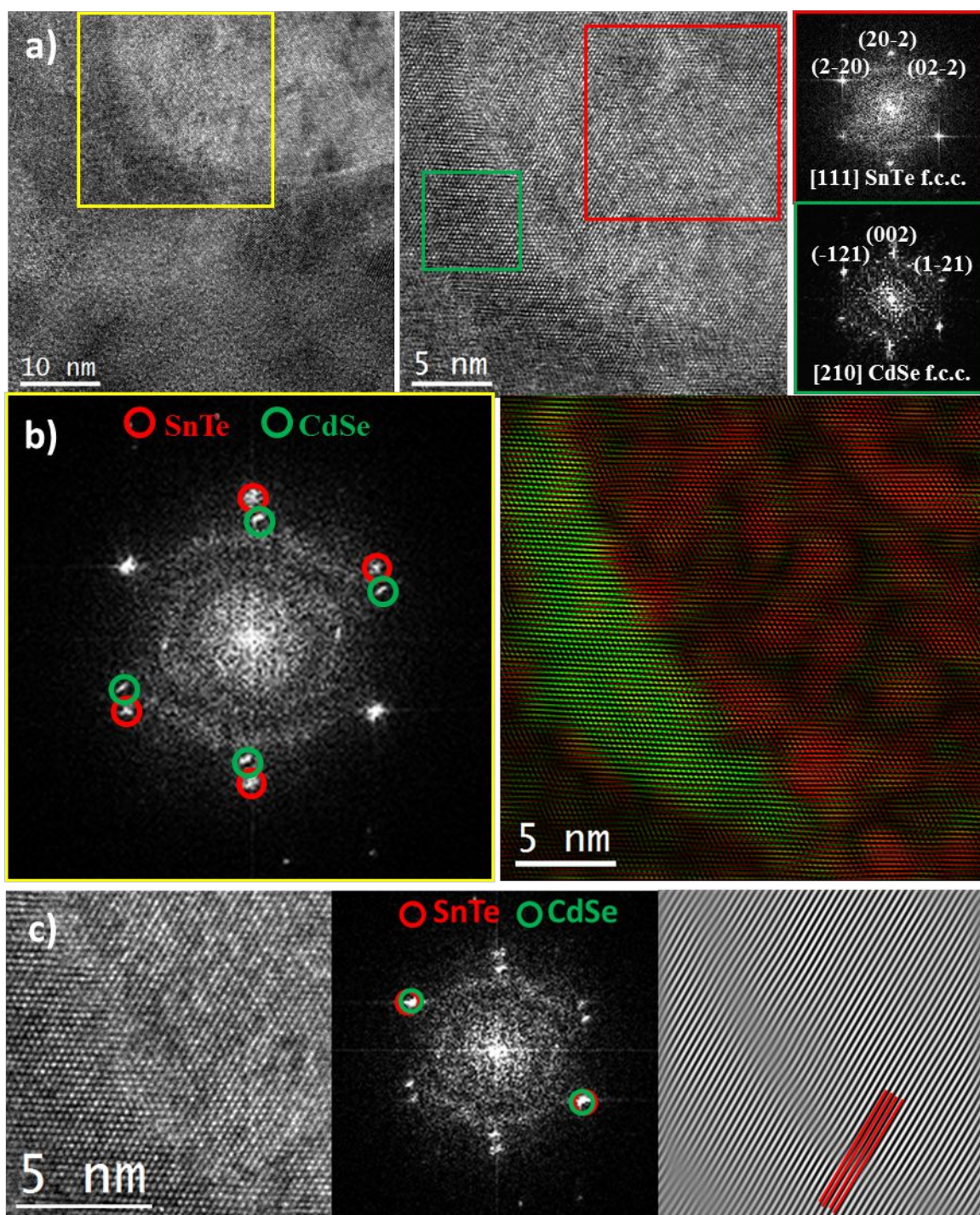**Figure S7:** Selection of HRTEM micrographs.

Figure S8. (Upper left) HRTEM micrograph obtained from the cross-section of the SnTe-CdSe pellet sample. (Upper middle) Detail of the yellow squared area. (Upper right) Power spectra (FFT) of the red squared (upper FFT) and green squared (lower FFT) regions from the HRTEM shown in the middle. (Lower left) FFT of the yellow squared region in the HRTEM shown in the upper left (i.e. general FFT of the HRTEM shown in the upper middle). (Lower right) False colored structural map of SnTe (red) and CdSe (green) phases obtained via filtering circled diffraction spots in the FTT. C) HRTEM image cut from the general image shown in a). Its corresponding power spectrum and inverse FFT of the selected diffraction spots. Almost a perfect epitaxy is formed between {220} planes of SnTe (d_{220} = 0.223 nm) and {211} planes of CdSe (d_{211} = 0.227 nm), with a lattice mismatch of ~1.8%. There is 1 SnTe plane for every CdSe plane.

Figure S8 shows detailed HRTEM investigation on a HRTEM micrograph shown in the upper left. As seen in this micrograph, it is taken from a junction of several grains. It can also be noticed here that there is segregation along the grain boundary of the upper right grain, acting as a shell for the grain. This particular region (yellow squared in the general HRTEM) is presented in detail in the HRTEM shown in the middle. Power spectrum obtained from the red squared region is shown in the right and revealed that the grain is composed of face centered cubic SnTe phase (space group = Fm3m) with a lattice parameter of 0.629 nm and it is visualized along its [111] zone axis. Another FFT is obtained from the green squared shell-like region and revealed that this region is composed of face centered cubic CdSe phase (space group = Fm3m) with a lattice parameter of 0.554 nm and it is visualized along its [210] zone axis. Lower row shows general FFT of the region of interest and false colored structural map of these two phases. The structural map is obtained by filtering two different diffraction spots for each phase as circled in the FFT. As clearly seen in the structural map, the grain is composed of SnTe and it is shell (or the crystalline region along the grain boundary of two larger grains) is composed of CdSe. Such a phase distribution is very much expected considering that this sample is fabricated via sintering of SnTe core - CdSe shell nanoparticles. Figure S8c shows that almost a perfect epitaxy is formed between {220} planes of SnTe (d_{220} = 0.223 nm) and {211} planes of CdSe (d_{211} = 0.227 nm), with a lattice mismatch of ~1.8%. There is 1 SnTe plane for every CdSe plane.
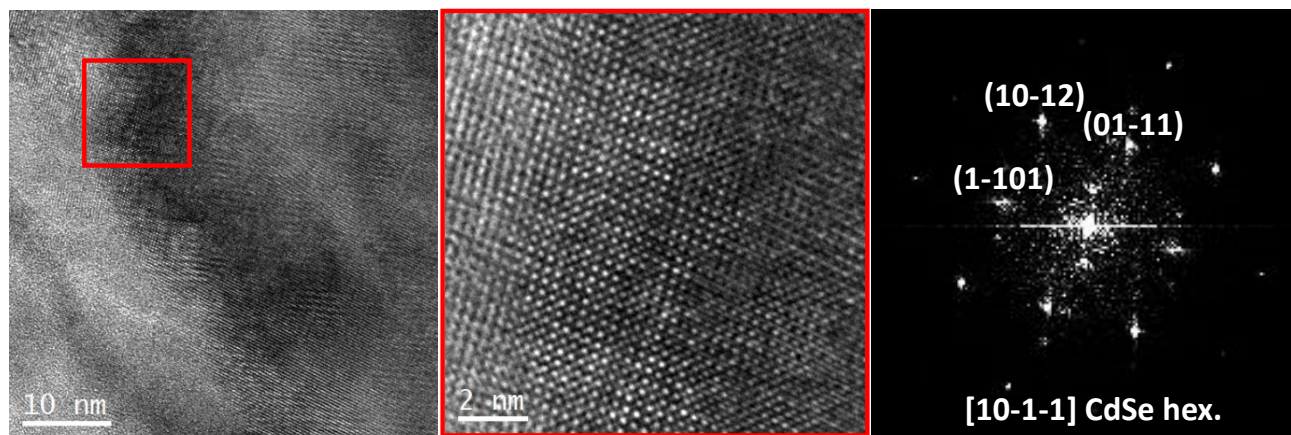

Figure S9. Example of a hexagonal CdSe precipitated. HRTEM micrograph showing a segregation-like region between two grain boundaries, detail of the region indicated with a red square and its corresponding power spectrum. Indexing for a hexagonal CdSe phase (space group = P6$_3$mc), with lattice parameters of a = 0.430 nm and c = 0.702 nm. It is visualized along its [10-1-1] axis.

6.3. Estimation of surface atoms and Cd content

We have estimated the number of atoms at the surface based on the material density and molar mass (Table S1).

Lattice constant (a)	0.63 nm
Avogadro constant (L)	6.022×10^{23} mol-1
Desnity (ρ)	6.44 × 10^{-21} g/nm^3
Molar mass (M)	246 g/mol
NP size (d); considering a cubic NP, side edge	14 nm
NP volume (V=d^3)	2744 nm^3
Total number of atoms in a NP (N = V × ρ × M^{-1} × L)	43259
NP surface volume (V$_S$=d^3-(d-a)^3)	354 nm^3
Atoms in the NP surface (N$_S$= V$_S$ × ρ × M^{-1} × L)	5581

Sn atoms in the NP surface ($N_S/2$)	2791
% of Sn surface atoms in the NP surface	6.4%

Table S1. Calculation of surface atoms in a 14 nm size SnTe NP.

The quantification of the Cd content in the nanocomposite was initially estimated based on the SnTe NC size and its density and molar mass. We considered that half of the atoms at the surface are Cd due to the ligand exchange, in a similar manner as previously reported for different systems such PbS (Chem. Mater. 2017, 29 (17), 7093-7097). Additionally, we perform ICP measurements, and the values obtained where similar to our calculations. For 14 nm SnTe NCs we found approximately 6.4% Cd. Based on X-ray diffraction data of the $Sn_{1-x}Cd_xTe$ system, the solubility limit of Cd in SnTe is around ~0.03 near room temperature s (J. Am. Chem. Soc., 2014, 136 (19), 7006–7017). Taking this into account, together with our experimental data (transport measurements, XRD and HRTEM), we believe that around 3% of Cd is alloyed and the remaining is present in the material as CdSe nanoprecipitates.
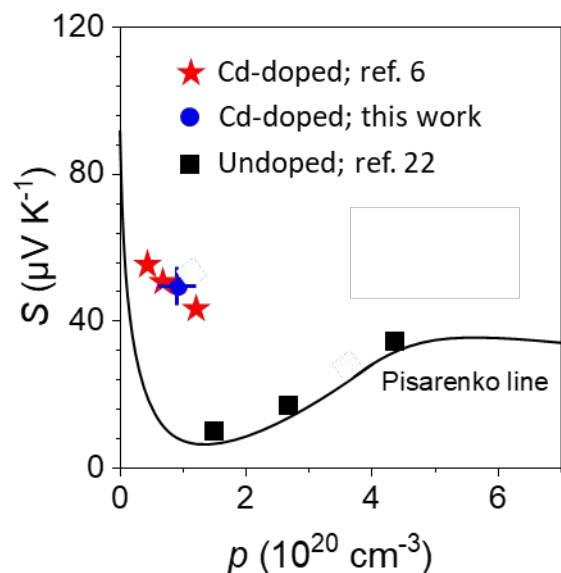
6.4. Pisarenko relationship

Figure S10. Room temperature Seebeck coefficient (*S*) as a function of carrier concentration (*p*) (Pisrenko plot). The black line is a theroretical prediction based on a VBM model.

6.5. SnTe-CdSe blending

We have mixed CdSe and SnTe NPs in solution and remove afterwards the solvent. The amount of CdSe NPs was chosen such that the final content of CdSe in the SnTe nanocomposite was the same as the one obtained in the nanocomposite produced with the CdSe-surface modified SnTe NP. Contradictory, the transport properties were very different. In fact the NP mixture presented similar results to bare SnTe nanomaterial. We attributed this to phase segregation between CdSe and SnTe which didn't allowed for the proper alloying of Cd to promote band converge.
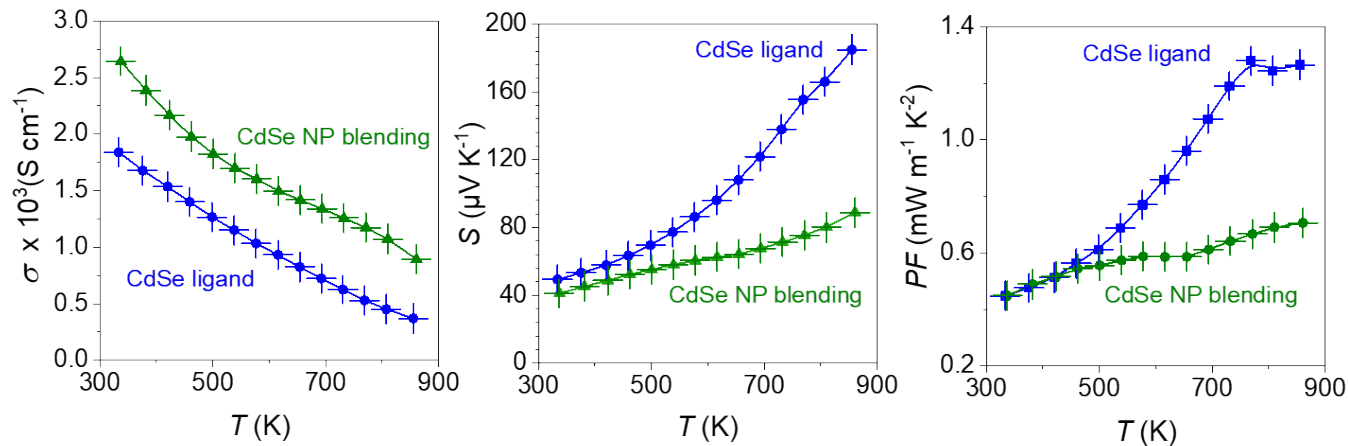
Figure S11. Electrical conductivity (right), σ; Seebeck coefficient (center), S; and power factor (left), PF for SnTe nanomaterial prepared with CdSe surface-modified SnTe NPs (blue) and a mixture of CdSe and SnTe NPs (green).

7. Table with the thermoelectric properties and corresponding ZT of state of the art SnTe-based materials

Values written on the table are mostly extracted from graphical data, therefore they can just be taken as the approximate value.

	System	σ (S cm^{-1})	S (μV K^{-1})	p (10^{20} cm^{-3})	PF (μW cm^{-1}K^{-2})	κ (W m^{-1}K^{-1})	κ_{latt} (W m^{-1}K^{-1})	ZT_{max}	T_{ZTmax} (K)	Ref.
Solid-state synthesis	$Sn_{0.96}Ga_{0.07}Te$	1200	178	3.3	25	2.27	0.48	1	873	[1]
	$Sn_{0.97}Bi_{0.03}Te$-3% SrTe	625	178	2.0	20	1.35	0.7	1.2	823	[2]
	$Sn_{0.555}Ge_{0.15}Pb_{0.075}Mn_{0.275}Te$	487	190	$\times$	17.6	1.13	0.38	1.42	900	[3]
	$Sn_{0.97}In_{0.015}Cd_{0.015}Te$-3%CdS	560	200	1.8	22.5	1.5	0.6	1.4	923	[4]
	$Sn_{0.94}Mn_{0.09}Te$	425	240	0.8	24.5	1.35	0.83	1.35	873	[5]
	$SnCd_{0.03}Te$-2%CdS	500	195	0.5	19	1.3	0.65	1.3	873	[6]
	$SnCd_{0.03}Te$-2%ZnS	500	180	0.5	16.2	1.3	0.65	1.1	873	[6]
	$SnTe–AgBiTe_2$	700	180	2	23	1.8	0.7	1.1	775	[7]
	$Sn_{0.96}Bi_{0.04}Te_{0.88}Cl_{0.12}$	690	182	1	22.9	1.55	0.8	1.27	873	[8]
	$SnAg_{0.025}In_{0.025}Te_{1.05}$	1150	165	2	31.4	2.72	1.17	1	856	[9]
	$(SnTe_{1-y}I_y)_{2.88}(In_2Te_{3-3y}I_{3y})_{0.04}$ y = 0.6%	900	165	3	25	2	0.6	1.1	923	[10]
	SnTe-17% MnTe	800	175	5	24	1.65	0.6	1.3	900	[11]

	$Sn_{0.98}Bi_{0.02}Te–3\%HgTe$	800	182	2.5	28	1.9	0.68	1.35	910	[12]
	$Sn_{0.94}Mg_{0.09}Te$	1000	175	2.4	30.3	2.2	0.78	1.2	860	[13]
	$Sn_{0.85}Sb_{0.15}Te$	1000	150	2.3	22.5	1.9	0.67	1	800	[14]
	$In_{0.015}Sn_{0.985}Te_{0.85}Se_{0.15}$	650	175	0.5	19	2.25	1.25	0.75	860	[15]
	$Sn_{0.88}Mn_{0.12}Te$	400	230	3.1	21	1.5	1	1.3	900	[16]
	$Sn_{0.94}Cu_{0.12}Te$	570	150	2.8	12.8	1.1	0.5	1	850	[17]
	$Sn_{0.905}Mn_{0.11}In_{0.005}Te$	310	240	1.2	17.8	1.27	0.9	1.15	823	[18]
Solution-processed	SnTe NP	1500	55	×	4	3	1.2	0.1	525	[19]
	165 nm SnTe Nps	450	90	4.4	3.64	0.6	0.2	0.5	803	[20]
	$Sn_{0.98}Cd_{0.02}Te_{0.90}Se_{0.10}$ particles	93	140	×	18.2	1.8	0.53	0.78	773	[21]
	SnTe-CdSe	380	185	0.9	12.6	0.85	0.48	1.3	853	This work

8. References

1. Al Rahal Al Orabi, R.; Hwang, J.; Lin, C.-C.; Gautier, R.; Fontaine, B.; Kim, W.; Rhyee, J.-S.; Wee, D.; Fornari, M., Ultralow lattice thermal conductivity and enhanced thermoelectric performance in SnTe: Ga materials. *Chem. Mater.* **2016,** 29, 612-620.

2. Zhao, L.-D.; Zhang, X.; Wu, H.; Tan, G.; Pei, Y.; Xiao, Y.; Chang, C.; Wu, D.; Chi, H.; Zheng, L.; Gong, S.; Uher, C.; He, J.; Kanatzidis, M. G., Enhanced Thermoelectric Properties in the Counter-Doped SnTe System with Strained Endotaxial SrTe. *J. Am. Chem. Soc.* **2016,** 138, 2366-2373.

3. Hu, L.; Zhang, Y.; Wu, H.; Li, J.; Li, Y.; Mckenna, M.; He, J.; Liu, F.; Pennycook, S. J.; Zeng, X., Entropy Engineering of SnTe: Multi-Principal-Element Alloying Leading to Ultralow Lattice Thermal Conductivity and State-of-the-Art Thermoelectric Performance. *Adv. Energy Mater.* **2018,** 8, 1802116.

4. Tan, G.; Shi, F.; Hao, S.; Chi, H.; Zhao, L.-D.; Uher, C.; Wolverton, C.; Dravid, V. P.; Kanatzidis, M. G., Codoping in SnTe: Enhancement of Thermoelectric Performance through Synergy of Resonance Levels and Band Convergence. *J. Am. Chem. Soc.* **2015,** 137, 5100-5112.

5. Guo, F.; Cui, B.; Liu, Y.; Meng, X.; Cao, J.; Zhang, Y.; He, R.; Liu, W.; Wu, H.; Pennycook, S. J., Thermoelectric SnTe with Band Convergence, Dense Dislocations, and Interstitials through Sn Self-Compensation and Mn Alloying. *Small* **2018,** 14, 1802615.

6. Tan, G.; Zhao, L.-D.; Shi, F.; Doak, J. W.; Lo, S.-H.; Sun, H.; Wolverton, C.; Dravid, V. P.; Uher, C.; Kanatzidis, M. G., High Thermoelectric Performance of p-Type SnTe via a Synergistic Band Engineering and Nanostructuring Approach. *J. Am. Chem. Soc.* **2014,** 136, 7006-7017.

7. Tan, G.; Shi, F.; Sun, H.; Zhao, L.-D.; Uher, C.; Dravid, V. P.; Kanatzidis, M. G., SnTe-AgBiTe2 as an efficient thermoelectric material with low thermal conductivity. *J. Mater. Chem. A* **2014,** 2, 20849-20854.

8. Zhou, Z.; Yang, J.; Jiang, Q.; Lin, X.; Xin, J.; Basit, A.; Hou, J.; Sun, B., Enhanced thermoelectric performance of SnTe: High efficient cation-anion Co-doping, hierarchical microstructure and electro-acoustic decoupling. *Nano energy* **2018,** 47, 81-88.

9.   Banik, A.; Shenoy, U. S.; Saha, S.; Waghmare, U. V.; Biswas, K., High Power Factor and Enhanced Thermoelectric Performance of SnTe-AgInTe2: Synergistic Effect of Resonance Level and Valence Band Convergence. *J. Am. Chem. Soc.* **2016,** 138, 13068-13075.

10.   Tan, G.; Zeier, W. G.; Shi, F.; Wang, P.; Snyder, G. J.; Dravid, V. P.; Kanatzidis, M. G., High Thermoelectric Performance SnTe–In2Te3 Solid Solutions Enabled by Resonant Levels and Strong Vacancy Phonon Scattering. *Chem. Mater.* **2015,** 27, 7801-7811.

11.   Wu, H.; Chang, C.; Feng, D.; Xiao, Y.; Zhang, X.; Pei, Y.; Zheng, L.; Wu, D.; Gong, S.; Chen, Y.; He, J.; Kanatzidis, M. G.; Zhao, L.-D., Synergistically optimized electrical and thermal transport properties of SnTe via alloying high-solubility MnTe. *Energy Environ. Sci.* **2015,** 8, 3298-3312.

12.   Tan, G.; Shi, F.; Doak, J. W.; Sun, H.; Zhao, L.-D.; Wang, P.; Uher, C.; Wolverton, C.; Dravid, V. P.; Kanatzidis, M. G., Extraordinary role of Hg in enhancing the thermoelectric performance of p-type SnTe. *Energy Environ. Sci.* **2015,** 8, 267-277.

13.   Banik, A.; Shenoy, U. S.; Anand, S.; Waghmare, U. V.; Biswas, K., Mg Alloying in SnTe Facilitates Valence Band Convergence and Optimizes Thermoelectric Properties. *Chem. Mater.* **2015,** 27, 581-587.

14.   Banik, A.; Vishal, B.; Perumal, S.; Datta, R.; Biswas, K., The origin of low thermal conductivity in Sn1-xSbxTe: phonon scattering via layered intergrowth nanostructures. *Energy Environ. Sci.* **2016,** 9, 2011-2019.

15.   Banik, A.; Biswas, K., Lead-Free Thermoelectrics: Promising Thermoelectric Performance in P-type $SnTe_{1-x}Se_x$ system. *J. Mater. Chem. A* **2014,** 2, 9620-9625.

16.   Tan, G.; Shi, F.; Hao, S.; Chi, H.; Bailey, T. P.; Zhao, L.-D.; Uher, C.; Wolverton, C.; Dravid, V. P.; Kanatzidis, M. G., Valence Band Modification and High Thermoelectric Performance in SnTe Heavily Alloyed with MnTe. *J. Am. Chem. Soc.* **2015,** 137, 11507-11516.

17.   Pei, Y.; Zheng, L.; Li, W.; Lin, S.; Chen, Z.; Wang, Y.; Xu, X.; Yu, H.; Chen, Y.; Ge, B., Interstitial Point Defect Scattering Contributing to High Thermoelectric Performance in SnTe. *Adv. Electron Mater.* **2016,** 2, 1600019-n/a.

18.   Wang, L.; Tan, X.; Liu, G.; Xu, J.; Shao, H.; Yu, B.; Jiang, H.; Yue, S.; Jiang, J., Manipulating Band Convergence and Resonant State in Thermoelectric Material SnTe by Mn–In Codoping. *ACS Energy Lett.* **2017,** 2, 1203-1207.

19.   Han, G.; Zhang, R.; Popuri, S.; Greer, H.; Reece, M.; Bos, J.-W.; Zhou, W.; Knox, A.; Gregory, D., Large-Scale Surfactant-Free Synthesis of p-Type SnTe Nanoparticles for Thermoelectric Applications. *Materials* **2017,** 10, 233.

20.   Li, Z.; Chen, Y.; Li, J.-F.; Chen, H.; Wang, L.; Zheng, S.; Lu, G., Systhesizing SnTe nanocrystals leading to thermoelectric performance enhancement via an ultra-fast microwave hydrothermal method. *Nano Energy* **2016,** 28, 78-86.

21.   Wang, L.; Chang, S.; Zheng, S.; Fang, T.; Cui, W.; Bai, P.-p.; Yue, L.; Chen, Z.-G., Thermoelectric Performance of Se/Cd Codoped SnTe via Microwave Solvothermal Method. *ACS Appl. Mater. Interfaces* **2017,** 9, 22612-22619.

22. Vedeneev, V.P., Krivoruchko, S.P. & Sabo, E.P. Tin Telluride Based Thermoelectrical Alloys. *Semiconductors*, **1998** 32: 241.